Saturn's innermost radiation belt throughout and inward of the D-ring

P. Kollmann[1], **E. Roussos**[2], **A. Kotova**[3], **L. Regoli**[4], **D. G. Mitchell**[1], **J. Carbary**[1], **G. Clark**[1], **N. Krupp**[2], **C. Paranicas**[1]

[1]Johns Hopkins University Applied Physics Laboratory, Laurel, MD 20723-6099, USA
[2]Max Planck Institute for Solar System Research, 37077 Göttingen, Germany
[3]IRAP, University de Toulouse, CNRS, UPS, CNES, Toulouse, France
[4]Department of Climate and Space Sciences and Engineering, University of Michigan, Ann Arbor, MI 48109-2143, USA

Key Points:

- We study Saturn's innermost radiation belt collocated with the D-ring that contains GeV protons
- The pitch angle distribution is shaped mostly by losses in atmosphere and ring
- Radiation measurements can be used to constrain exospheric and D-ring densities

This is the author manuscript accepted for publication and has undergone full peer review but has not been through the copyediting, typesetting, pagination and proofreading process, which may lead to differences between this version and the Version of Record. Please cite this article as doi: 10.1029/2018GL077954

Abstract

Cassini discovered Saturn's innermost radiation belt during the end of its mission. The belt is populated with relativistic protons, probably up to the trapping limit of ≈ 20GeV. It extends from Saturn's dense atmosphere into and throughout the D-ring. The A-C-rings separate this belt entirely from the previously known radiation belts, suggesting that the innermost radiation belt is populated entirely via cosmic ray albedo neutron decay. We find that the proton pitch angle distributions are consistent with being shaped by losses to the D-ring and the upper atmosphere rather than for example wave-particle interactions. This supports that the main loss process of this new radiation belt is energy loss in neutral material, different from Saturn's other radiation belts. This property constrains the overall scale height of Saturn's exosphere to < 700km and the average D-ring water molecule column density to being about one order of magnitude below the Enceladus gas torus.

Plain Language Summary

A fundamental property that a planet with a magnetic field can have is if it is encompassed by radiation belts of energetic ions and electrons approaching light speed. It was the first discovery of the space age that this is the case for Earth. For Saturn, the Cassini satellite recently discovered an unknown radiation belt trapped between the planet and its rings. The physics of this radiation belt is as different to Saturn's previously known radiation belts, as Saturn's belts differ from Earth's. Here we seek the reason why the proton intensities in this new belt do not rise to extremely high values. We find that this is because the densities of Saturn's high atmosphere and inner rings are sufficiently high to deplete the protons as fast as they are produced.

1 Introduction

Saturn's proton radiation belts show properties that are unique in our solar system and make them an ideal test bed to study some aspects of radiation belt physics. Radiation belts other than Saturn's proton belts are populated with particles from various sources, including particles that were accelerated in the magnetosphere and then radially transported inward. These mechanisms can be difficult to disentangle. At Saturn, such radial transport is efficiently blocked by the moons and main rings [*Roussos et al.*, 2008; *Kollmann et al.*, 2013]. Since Saturn's radiation belts therefore cannot be supplied by magnetospheric ions, their dominant source process for MeV and GeV protons is the decay of secondary neutrons produced by cosmic rays impacting neutral material around Saturn. This so called CRAND process (cosmic ray albedo neutron decay) is especially efficient thanks to Saturn's dense main rings [*Hess et al.*, 1961; *Cooper*, 1983; *Kotova et al.*, 2018].

The intensity of Saturn's radiation belts between the F-ring and the orbit of Tethys is limited by radial diffusive transport into the moon and ring orbits. Radial diffusion explains the intensity profiles measured during one orbit [*Cooper*, 1983; *Kollmann et al.*, 2013] and the year-long intensity modulation [*Kollmann and Roussos et al.*, 2017].

It took until the end of the Cassini mission in 2017 to finally observe Saturn's innermost radiation belt [*Roussos and Kollmann et al.*, 2018]. The dominant population of the belt is MeV and GeV protons. The belt extends from the D73 ringlet to Saturn's dense atmosphere. Cassini was able to measure protons trapped in the D-ring while being magnetically connected to it from high latitudes. It was not necessary to actually fly vertically through the D-ring itself. Since charged particles continuously bounce through the D-ring, they are much more sensitive to the ring density than light, which only passes through a ring once.

The presence of Saturn's innermost radiation belt was predicted earlier [*Van Allen et al.*, 1980; *Cooper*, 2008; *Kollmann et al.*, 2015], where it was suggested that its intensity profiles would be determined by different physics than for the belts outside of the rings: the loss mechanism of the innermost belt would not be radial diffusion but local energy loss in the D-ring and the atmosphere that affects also particles that do not reach the loss cone.

The measurements during Cassini's last orbits are discussed in Sec. 2. The main topic of the current paper is the first quantitative data analysis. We discuss the coupling of the proton radiation belts with the D-ring and the upper atmosphere (Sec. 3) and use this to estimate the density of the inner D-ring (Sec. 5).

2 Data

Our analysis is based on data from the LEMMS instrument (low energy magnetospheric measurement system, *Krimigis et al.* [2004]). The raw data from the innermost radiation belt are described in *Roussos and Kollmann et al.* [2018] and *Krupp et al.* [2018]. We summarize the key points in S.1.1 in the supporting online material (SOM) and show raw counts in SOM S.1.5.

To convert the measured raw count rates into physically meaningful intensities we follow the same technique as in *Roussos and Kollmann et al.* [2018], where we assume an intensity distribution j, calculate the expected count rates R_r, compare them to the measured count rates R_m, and change the assumption until the discrepancy Δ (see Eq. 3) reaches a minimum and is small. Sample comparisons between R_r and R_m for different assumptions discussed below are provided in SOM S.1.6 to S.1.10. Forward modeling is similar to performing curve fitting. The difference is that we fit intensities to counts instead of intensities to intensities.

We assume that j can be described as

$$j(\alpha_{eq}, E) = j_A J(\alpha_{eq}) \mathcal{A}(E) \tag{1}$$

where j and j_A are differential intensities and J and $\mathcal{A}$ are dimensionless quantities. The pitch angle distribution (PAD) $J(\alpha_{eq})$ is assumed to be independent of energy, which is reasonable since PAD shapes commonly stay similar for wide energy ranges [*Roussos et al.*, 2011; *Clark et al.*, 2014]. The PAD will be discussed throughout Sec. 3. The energy dependence $\mathcal{A}$ is

$$\mathcal{A}(E) = \left(\frac{E}{E_0}\right)^{\gamma} \frac{1}{1 + \exp\big((E - E_C)/K_T\big)} \tag{2}$$

where we fix $E_0 = 39$MeV without loss of generality. The energy dependence follows a power law in energy that cuts off sharply at energy E_C. Power laws with some sort of cutoff or roll over are common in radiation belts [*Garrett et al.*, 2012; *Selesnick et al.*, 2014; *Adriani et al.*, 2015]. The sharpness of the cutoff is assumed as $K_T = 0.05 E_C$. The forward model requires $E_C > 1$GeV, implying that the spectrum may extend up to the trapping limit at 20GeV (*Roussos and Kollmann et al.* [2018], Fig. S.7). We therefore fix $E_C = 20$GeV.

All free parameters (j_A, γ, and the implicit parameters in J) are independently determined for each L-shell. The power law exponent is found to be $-1.3 < \gamma < -0.7$ (see SOM S.1.11A). Fixing γ to a value in this range still yields reasonable results but larger errors. Other parameters are discussed in Sec. 3.

The difference between modeled and measured rate is quantified via the root-mean-square error Δ.

$$\Delta = \sqrt{\sum_i^I (\delta_i)^2 \Big/ I} \tag{3}$$

with $\delta_i = \log R_r^i - \log R_m^i$, where i runs over all I measurement bins at the given L-shell. Minimized Δ values are provided in SOM S.1.11C and more details on the forward modeling in general in SOM S.1.2.

3 Pitch angle distribution shaped by neutral material interaction

The forward model that we use to retrieve intensities from the raw counts (Sec. 2) relies on assuming a shape of the PAD. Throughout the following sections, we will assume various PAD shapes and show and discuss the resulting intensities.

The varying success of fitting with different PAD shapes will provide insights into the physics of Saturn's innermost radiation belt. Generally, PADs may be shaped by diffusion in pitch angle that drives particles into the dense atmosphere [*Selesnick et al.*, 2003]. Since energetic protons are barely scattered while being stopped in matter [*Ziegler*, 2008; *Kollmann et al.*, 2013], pitch angle diffusion can only result from wave-particle interactions. We will demonstrate that such waves are not necessary to reproduce the data.

3.1 Phenomenological PAD

We start without implying any physics by assuming a purely phenomenological PAD

$$J(\alpha_{eq}) = \frac{1 + \exp\left((C - \alpha_0)/k_t\right)}{\sin^N \alpha_0} \frac{\sin^N(\alpha_{eq})}{1 + \exp\left((C - \alpha_{eq})/k_t\right)} \tag{4}$$

The value of $\alpha_0 = 90°$ is chosen without loss of generality. A Sine-function to the power of N is a common description of PADs [*Rymer et al.*, 2008; *Clark et al.*, 2014] and was applied earlier to this data [*Roussos and Kollmann et al.*, 2018].

The PAD drops into the loss cone below angle C. We assume that this drop is abrupt by selecting $k_t = 0.18°$. Results are not sensitive to k_t as long as k_t is small. The geometric loss cone C is the largest equatorial pitch angle where charged particles enter Saturn's 1-bar surface before magnetically mirroring. We calculate C based on conservation of the first adiabatic invariant during the bounce motion [*Roederer*, 1970] through tracing in our magnetic field model to both poles, taking into account Saturn's oblateness (equatorial radius 60268km= $1 R_S$, polar radius 58232km, *Seidelmann et al.* [2007]). Since particles entering the loss cone are lost very efficiently, the intensity inside the loss cone is usually negligible.

Figures/Fig1_PAD.pdf

Figure 1. Equatorial pitch angle distributions (PADs) of 300MeV protons based on the raw data and forward models assuming different PADs. Vertical lines indicate the geometric loss cone angle below which particles reach Saturn's 1-bar surface. The "lower limit" atmosphere is based on *Koskinen et al.* [2013] and fits the raw count rates well. The "upper limit" is provided by the Cassini atmosphere engineering model. We do not consider the best fit from the "upper limit" atmosphere (red) as a good fit. Other models that are unlikely or have poor fits are not shown for clarity. The discrepancy Δ provided in the legends is defined in Eq. (3).

We find that the phenomenological PAD fits the observed count rates. A sample comparison between measured and phenomenologically modeled count rates is provided in SOM S.1.7. Figure 1 shows modeled PAD intensities for L-shells within the D-ring and within Saturn's exosphere. It can be seen that these PADs cover several orders of magnitude in intensity even before reaching the loss cone. Such a change is unusually steep compared to Saturn's magnetosphere beyond the rings, where intensity changes with pitch angle well below an order of magnitude are the norm [*Clark et al.*, 2014]. The reason for this steepness is discussed below.

3.2 PAD from interaction with atmosphere

We hypothesize that the steep change in intensities even outside the loss cone is a result of the interaction with Saturn's exosphere. Already before a particle reaches the high densities at the 1-bar surface, it interacts with the exosphere above that.

Charged particles traversing the neutral material of an atmosphere, ring, or gas torus lose energy. This energy loss modifies the shape of the energy spectrum, often in a way that the intensity at each energy is decreasing, which is why we will often refer to the energy loss also as a particle loss. The quantitative relation between charged particle intensity and neutral density has been derived and used in previous studies [*Kollmann et al.*, 2013, 2015, 2016]. We summarize the derivation and discuss its application to the used data in SOM S.1.4. The main assumption, which turns out to reproduce the data well, is that the PAD $J(\alpha_{eq})$ is energy independent. Any kind of energy dependence therefore affects the absolute value of $j(E, \alpha_{eq})$ but not the relative change of $J(\alpha_{eq})$ with pitch angle at any given energy. With this in mind, the final relation between intensity and neutral density is

$$j(E, \alpha_{eq}) \propto J(\alpha_{eq}) = \frac{n_A}{\widetilde{n}(\alpha_{eq})} \tag{5}$$

n_A is a scaling factor with the dimension of a number density. $\widetilde{n}$ is the bounce-averaged neutral material density that a charged particle is exposed to over its bounce time T_B [*Walt*, 1994], which is different to the density n at a single location in space. $\widetilde{n}$ accounts for the local density significantly changing along the particle trajectory and weights the density by the time the particle spends in it. Since the particle stays relatively long near its mirror points, high latitude densities are highly weighted.

$$\widetilde{n}(L, \alpha_{eq}) = \frac{\int_0^{T_B} n\big(\vec{r}(t)\big)\ \mathrm{d}t}{T_B} \tag{6}$$

$\vec{r}(t)$ describes the particle location over time t during its bounce motion.

Note that the bounce-averaged density $\widetilde{n}$ is a function of pitch angle and solely responsible here for the shape of the pitch angle distribution J. For equatorially mirroring pitch angles, $\widetilde{n}$ equals the equatorial density. More field-aligned pitch angles reach into deeper atmospheric layers. This makes $\widetilde{n}$ rise and j decrease with falling α_{eq}, which shows that the shape of the pitch angle distribution $j(\alpha_{eq})$ reflects the shape of $1/n(r)$, the inverse of the atmospheric altitude profile. This behavior naturally creates a loss cone, even though its onset can deviate by $< 10°$ from the geometric loss cone. Since this deviation is likely a result of our current determination of $\widetilde{n}$ through a simple magnetic dipole model, while we use a third order model to determine the geometric loss cone, we use $\widetilde{n}$ from a neighboring L-shell to shift the loss cone to its expected location.

To calculate $\widetilde{n}$, we use the H_2 exosphere of scale height 200km determined by *Koskinen et al.* [2013] and the dense H_2 atmosphere by *Shemansky and Liu* [2012] (Fig. 2C). We term this our "lower limit" model, as explained below. A H corona, plume [*Shemansky et al.*, 2009], or ionosphere [*Nagy et al.*, 2009] are not included in this first attempt, nor do we account for latitude or time dependencies [*Koskinen et al.*, 2015].

After selection of the atmospheric profile, our free parameters are the overall intensity, now described by the product $j_A n_A$, and the spectral slope γ (see Eq. 1). One example PAD resulting from this atmosphere is shown in Fig. 1A. The "lower limit" density model fits the raw data almost as well as the phenomenological PAD from Sec. 3.1, as quantified with Δ.

In order to test how sensitive the energetic protons are to the atmosphere model, we also try another model. The "upper limit" model, namely the Cassini project engineering atmosphere model [*Strobel*, 2015] that is based on data from *Koskinen et al.* [2013, 2015], mostly adds a H corona with upper limit densities, see Fig. 2C. This model was designed to predict when Cassini would start tumbling during its last orbits and therefore works best in the dense atmosphere. At altitudes above its specified validity range, it has an H corona based on a ratio of $H/H_2 = 0.05$ at the exobase, meaning that its H density is an upper limit. The H has a scale height of 700km, which is longer than Saturn's H_2 exospheric scale height but shorter than Jupiter's H corona with 1000km scale height [*Gladstone et al.*, 2004].

The "upper limit" model with its slowly changing density over distance yields PADs that change similarly slowly with pitch angle outward of the loss cone. An example of such a PAD is shown in Fig. 1A. Even though we show the best fit to the data here, this is not a good fit. Slowly changing PADs are not consistent with the proton data and the error of the forward model using the "upper limit" atmosphere is on average 2.5 times as large as of the other models (see Fig. S8C). We will therefore not use results based on the "upper limit" model in the following.

We refer to the models as upper and lower limits since assuming no H corona at all and assuming a dense corona brackets Saturn's actual exosphere. Testing both demonstrates that the proton measurements are sensitive enough to at least rule out some reasonable exospheric models. The proton data is more consistent with the assumption of no corona than of a dense corona. While this does not rule out a corona, it suggests that the corona is tenuous or of a scale height comparable to the H_2 exosphere. Future analysis will refine this constraint.

3.3 PAD from interaction with D-ring

Running the forward model for the entire innermost radiation belt shows that the PADs change with distance, independent of what function is used to describe them: Moving from small L into the D-ring shows that the phenomenological PADs become more isotropic in the D-ring (illustrated in SOM S.1.11B). The D-ring is also the region where PADs shaped only by losses to the atmosphere do not fit the data well. (The "lower limit" model reaches errors $\Delta > 0.1$ for $L > 1.09$ and is discarded for larger distances, see SOM S.1.11C.) These findings suggest that additional losses to the D-ring are needed to reproduce D-ring data.

Interaction with the D-ring can formally be calculated as for the atmosphere (Eq. 5). The only difference is the scaling of the bounce-averaged density $\widetilde{n}$ with pitch angle. For the atmosphere, this density is highest for field-aligned protons that dip into the denser atmosphere. For a ring, $\widetilde{n}$ is highest for equatorially mirroring protons that spend all their time close to the ring. (Exactly equatorial particles never encounter the ring plane due to the small offset of the magnetic equator [*Burton et al.*, 2010]. Since these particles never reach Cassini, we ignore the offset here.)

In order to calculate $\widetilde{n}$ to determine the PAD, we assume that the D-ring is a slab of constant density n, meaning that its ice grains are spread out into a homogenous gas. This treatment would break down if a significant fraction of grains or boulders in the ring stops a proton already after a small number of impacts [*Kollmann et al.*, 2015]. It requires mm-sized grains to affect our lowest and m-sized grains to affect our highest energy protons. We do not expect a high abundance of either in a tenuous ring [*Hedman et al.*, 2007], so that our approach is applicable here.

Figures/Fig2_radial.pdf

Figure 2. Panel A: 300MeV proton intensities in Saturn's innermost radiation belt as a function of L-shell, which measures distance in multiples of Saturn radii ($1R_S = 60268$km). Intensities are from forward models constrained by measured data. Error bars span the range resulting from different assumptions used for the forward models (Sec. 3). X-symbols mark our best guess intensity (explained in Sec. 4.1). The radiation belt likely extends down to $L \approx 1.03$ but there are not enough data below $L = 1.05$ to run our forward model. While the intensities for $\alpha_{eq} = 90°$ protons are not well constrained, their difference to the 80° intensities illustrates the change in PAD shape between the D-ring and the exosphere. Panel B: Similar as panel A but for omnidirectional intensities. The highest energy protons have 1-20GeV in this belt. Panel C: Neutral molecule densities. Densities are particles per volume and provided in Saturn's equatorial plane unless stated otherwise in the legend. The "lower limit" model only includes H_2, the "upper limit" model combines H_2 with a dense H corona (Sec. 3.2). D-ring densities are derived in Sec. 5. Ringlet densities are estimated based on the depth of the proton intensity depletion (Sec. 4.2).

We assume a latitudinal extent of the ring equivalent to a thickness $H = 100$m at $L = 1.17$, an order of magnitude above the A-ring thickness [*Charnoz et al.*, 2009]. The bounce-averaged density $\widetilde{n}$ from Eq. (6) becomes for a ring

$$\widetilde{n} = n\frac{T_r}{T_B} \approx \frac{nH}{v_{\parallel}T_B} \tag{7}$$

T_r is the time the particle spends in the ring and $v_{\parallel}$ its velocity parallel to the magnetic field while in the ring plane. The product nH is the water molecule column density. The approximation in Eq. (7) is true if the pitch angle is field aligned enough and the ring thin enough so that $v_{\parallel}$ does not significantly change within the ring. This is the case: Even the most equatorial pitch angles reaching LEMMS from the D-ring, $\alpha_{eq} \approx 70°$, would require the ring to be thicker than $H > 0.2R_S$ to change $v_{\parallel}$ by a factor of > 2.

Combining Eqs. (1), (5), and (7) yields

$$j \approx j_A \frac{n_A\ v_{\parallel}T_B}{nH}\mathcal{A} \tag{8}$$

Free parameters in the forward model are the product $(j_A n_A)/(nH)$ and γ. We calculate the value of nH, without the other factors, in Sec. 5.

Figure 1B shows an example PAD resulting from combining atmospheric and D-ring losses. The main difference to the phenomenological PAD is the low intensity for $\alpha_{eq} = 90°$. This model fits the data slightly better than the phenomenological model (compare Figs. S.1.9 with S.1.10 and their Δ). We therefore consider this model as the most likely one and conclude that the PADs are consistent with being solely determined by losses in atmosphere and ring.

The data inward of the D-ring edge can be reproduced by either assuming a much smaller density than in the bulk of the D-ring or by assuming no ring at all. This means that the proton data cannot be used to measure the gradual decay of the D-ring inward of its inner edge that is suggested by the normalized I/F reflectance [*Hedman et al.*, 2013].

4 Discussion of loss processes

4.1 D-ring and atmosphere

An overview of different forward model results is provided by Fig. 2A-B, showing intensities as a function of L-shell for different energies and pitch angles. Only models with errors $\Delta < 0.1$ are included. The error bars provide the intensity range covered by the various models. X-symbols mark the best guess intensities: Within the D-ring, the best guess uses the model that has the best fit, is physics-based and suggests proton losses in the D-ring. Within the exosphere, the best guess averages over the model results since their fits and assumptions are similarly good.

The intensities rise with increasing distance to Saturn in a similar way as the loss rate in the exosphere decreases. The intensities do not keep rising after reaching the D-ring but level off instead. This suggests that energy loss in the D-ring limits the intensities and that the D-ring has a constant density, except at its ringlets discussed in Sec. 4.2.

Except for equatorially mirroring protons, we find the intensities to peak at $L_p \approx 1.09$. We already suggested in *Kollmann et al.* [2015] that there would be a location in the range $1 < L < 1.1$ where the combined proton losses due to ring and exosphere reach a minimum. Since neutral density and proton intensity are inversely proportional to each other (Eq. 5), the density minimum leads to an intensity maximum. We will use this behavior to estimate the D-ring density in Sec. 5.

We are not able to constrain the intensity of equatorially mirroring protons to a high degree of certainty since measuring this population requires Cassini to traverse the equatorial plane, which only occurred in the range $1.04 < L < 1.06$. Nevertheless, low intensities of $\alpha_{eq} \approx 90°$ protons and adjacent pitch angles provide a better fit to the data than high intensities (Fig. 1B). The change in equatorial intensities between the D-ring and the region inward of the D-ring is a good illustration for the change in the PAD shape with L-shell and allows us to rule out an alternative explanation for the low intensities of near-equatorial protons. In principle, low equatorial intensities may result from the source if it is dominated by CRAND from the rings: CRAND neutrons from the rings cannot populate pitch angles close to the magnetic equator because the rings are very close to the magnetic equator and will stop neutrons moving through the ring plane. However, such shadowing would deplete the equatorial intensities at all L, not just throughout the D-ring.

In summary, the main loss process determining the radial and pitch angle distributions is local energy loss in neutral material. Pitch angle diffusion into atmospheric material and the source's PAD play no major role.

4.2 Ringlets

The D-ring is highly structured. Most notably it includes three ringlets referred to as D68, D72, and D73, as well as the outer, more dense D-ring, right outward of D73 [*Hedman et al.*, 2007]. Yellow shaded areas in Fig. 2 illustrate either the width of the ringlet or the radial extent that it covers (for example due to an elliptic orbit), depending on what is larger.

It can be seen that the D68 ringlet depletes the proton intensities by a factor of $\approx$ 10, with the exact value depending on energy. This suggests that D68 has a higher water molecule column density than the bulk D-ring. Note that the proton drift through the ringlet will average over the longitudinal asymmetries present in the ringlet [*Hedman et al.*, 2007]. The alternative to a higher density is the presence of meter-sized boulders or moonlets that absorb protons at the first encounter, different to the smaller grains we assume for the D-ring. The locations of intensity minimum and ringlet center deviate by $\approx 0.005R_S$, which may be due to the used magnetic field model.

Interestingly, the width of the depletion of GeV protons (Fig. 2B, orange curve) is broader than the radial extent of the ringlet, even when accounting for long-term changes in the ringlet location [*Hedman et al.*, 2014]. At MeV energies (blue), the signature of the D68 ringlet is subtle. The gyroradius of a charged particle makes the effective area where the particle can be absorbed larger than the absorbing body or ring. The gyroradius of GeV protons is of the order of $0.01R_S$. Since this is similar to the width of the D68 absorption feature at GeV energies, it suggests that the gyroradius is responsible for the broadness of the depletion. The gyroradius is an order of magnitude smaller at MeV energies and therefore similar to the extent of the D68 ringlet. This is less than we can resolve and therefore consistent with the absence of a notable absorption at MeV energies.

There are alternative explanations for the width and energy dependence of the ringlet dropouts: the broad depletion may result from radial diffusion, like in Saturn's outer proton belts that show intensity reductions already outward of the moon orbits. However, the diffusion coefficient follows $D_{LL} \propto L^{10}$ outward of the main rings [*Cooper*, 1983; *Kollmann and Roussos et al.*, 2017], which yields negligible D_{LL} values if it can be extrapolated to the innermost belt [*Kollmann et al.*, 2015].

Interestingly, the D72 ringlet does not cause significant proton absorption. While infrared and visible observations suggest differences in the grain size distribution and composition of D-ring and D72 ringlet [*Hedman et al.*, 2007], our proton data suggests that their column densities are comparable.

All intensities are low within the outer D-ring, suggesting a high density in this region, which is consistent with this being the only part of the D-ring where the optical depth could be determined [*Hedman et al.*, 2007]. The outer D-ring is wide enough that all measured protons can be immersed in it, irrespective of their gyroradius. The onset of the absorption already starts outward of the neighboring D73 ringlet for GeV energies, consistent with this resulting from a large gyroradius. At MeV energies, the intensities are consistent with following an abrupt change at the D73 boundary that is smeared out by our L-shell determination and binning.

5 D-ring density estimate

Both the exosphere and the D-ring remove protons. We use the fact that the proton loss rate (change of proton phase space density per time) due to the D-ring increases towards the ring, while the loss rate due to the exosphere decreases with distance to Saturn. Adding a rising function to a falling function yields a function with a minimum where both functions are equal. We will call the location where the total loss rate reaches its minimum L_p. At L_p, the loss rates of ring and exosphere are equal:

$$\left.\frac{\mathrm{d}f}{\mathrm{d}t}\right|_{\mathrm{rng}} = \left.\frac{\mathrm{d}f}{\mathrm{d}t}\right|_{\mathrm{exo}} \tag{9}$$

The loss rates can be calculated through Eq. (18) in the SOM. Inserting the intensities from our forward model and using energy loss values for a pure H_2 exosphere and a ring of H_2O ice we get (see SOM S.1.4) for our energy range

$$\widetilde{n}_{\mathrm{rng}} \approx \widetilde{n}_{\mathrm{exo}}/0.2 \tag{10}$$

We apply Eq. (6) to the “lower limit” atmosphere (that fits the data best) and find that the bounce-averaged density $\widetilde{n}_{\mathrm{exo}}$ only differs by a factor of 2 from the equatorial density n_{exo} at L_p:

$$\widetilde{n}_{\mathrm{exo}} = 2n_{\mathrm{exo}} \quad \text{for } \alpha_{eq} = 80^\circ \tag{11}$$

Assuming a D-ring with parameters as in Sec. 3.3 and applying Eq. (7) yields a large difference between bounce averaged and equatorial densities in case of the D-ring:

$$\widetilde{n}_{\mathrm{rng}} = 9 \times 10^{-6}\ n_{\mathrm{rng}} \quad \text{for } \alpha_{eq} = 80^\circ \tag{12}$$

We identify $L_p \approx 1.09$ as the location of minimum loss rate because this minimum goes along with the observed maximum in $\alpha_{eq} = 80^\circ$ intensity. The exospheric neutral density at L_p based on our "lower limit" model is $\widetilde{n}_{\mathrm{exo}} = 9 \times 10^7/\mathrm{m}^3$ [*Koskinen et al.*, 2013]. Since this density would change by an order of magnitude when L_p is modified by $0.01 R_S$, the following estimates need to be considered with caution. With Eqs. (10) and (12) the water molecule number density of a $H = 100$m thick ring at L_p, inward of the D-ring edge is $n_{\mathrm{rng}} = 5 \times 10^{13}/\mathrm{m}^3$. We assume that the density increases exponentially with a scale length of 1000km until the D-ring edge, as suggested by the optically observed normalized I/F [*Hedman et al.*, 2013]. This increase is consistent with the L-dependence we find for the proton intensities. The estimated density at $L = 1.11$, in the D-ring, is therefore $n_{\mathrm{rng}} \approx 2 \times 10^{14}/\mathrm{m}^3$. Since we cannot distinguish dense thick and tenuous thin rings, more robust than n_{rng} and H is the column density $nH = 2 \times 10^{16}/\mathrm{m}^2$. For comparison, this column density is an order of magnitude lower than for the Enceladus neutral gas torus collocated with the E-ring [*Hartogh et al.*, 2011].

n_{rng} are water molecule densities averaged over the ring volume. In reality, the water is clustered into ice grains. If all grains have the same radius a, the number of grains per volume $\bar{\bar{n}}$ can be calculated with

$$n_{\mathrm{rng}} = \frac{\rho}{M}\frac{4\pi}{3}a^3\bar{\bar{n}} \tag{13}$$

ρ is the mass density of the water ice grains that we assume here as $\rho = 10^3\mathrm{kg/m}^3$ and M the mass of a water molecule. If we assume $a = 1\mu$m, the typical size for the inner D-ring [*Hedman et al.*, 2007], we get $\bar{\bar{n}} \approx 1 \times 10^3/\mathrm{m}^3$. This is 10^4 times higher than for μm-grains in the E-ring [*Kempf et al.*, 2008].

More realistic than assuming a single grain size is the use of a distribution function $\bar{n}$, describing grains of radius a per volume and radius interval. We assume

$$\bar{n} = \bar{n}_0 \left(\frac{a}{a_0}\right)^{-3} \tag{14}$$

as it is typical for rings [*Charnoz et al.*, 2009]. The average water density n_{rng} then becomes

$$n_{\mathrm{rng}} = \frac{\rho}{M}\int_{a_{\min}}^{a_{\max}} \frac{4\pi}{3}\bar{n}a^3\ \mathrm{d}a = \frac{\rho}{M}\frac{4\pi}{3}\bar{n}_0 a_0^3 (a_{\max} - a_{\min}) \tag{15}$$

Since a direct observation of the ring density can only be performed by entering the D-ring, we relate it to the optical depth τ, which can be observed remotely.

$$\tau = \int_{a_{\min}}^{a_{\max}} \overline{n} H \pi a^2 \, \mathrm{d}a = \overline{n}_0 H \pi a_0^3 \Big(\ln(a_{\max}) - \ln(a_{\min}) \Big) \quad (16)$$

H is the ring thickness. We solve Eq. (15) for $\overline{n}a_0^3$. Introducing $\overline{n}a_0^3$ into Eq. (16), using our n_{rng} value, and assuming $H = 100\mathrm{m}$, $a_{\max} = 1\mu\mathrm{m}$, and $a_{\min} = 0.1\mathrm{nm}$ yields $\tau \approx 4 \times 10^{-6}$. This is consistent with optical observations showing $\tau < 10^{-3}$ for the inner D-ring [*Hedman et al.*, 2007]. Future analysis should be able to further constrain the D-ring density.

6 Summary

1. This paper analyzes data from Saturn's innermost radiation belt. The following properties were already known from previous studies [*Roussos and Kollmann et al.*, 2018]: It is populated by protons with at least 25MeV and potentially up to 20GeV. It is located between the D73 ringlet and Saturn's dense atmosphere ($1.03 < L < 1.23$, see also Fig. 2A) and clearly separated by Saturn's A-C-rings from the already known proton belts ($2.27 < L < 4.9$).
2. The pitch angle distributions of the innermost belt are consistent with being shaped by losses in the exosphere and the D-ring (Fig. 1). Pitch angle diffusion is at most a secondary effect.
3. From high to low altitudes, the inferred intensities are relatively uniform throughout the L-shells of the D-ring, show a maximum at $L \approx 1.09$, where the combined losses from ring plus exosphere reach their minimum, and decrease towards Saturn's dense atmosphere (Fig. 2).
4. We conclude based on 2. and 3. that the main loss process of the innermost radiation belt is local energy loss in neutral material. This is in strong contrast to the proton belts outward of the main rings, where the main loss process is radial diffusion [*Kollmann and Roussos et al.*, 2017].
5. The proton pitch angle distributions indicate that the overall scale height of all species in Saturn's exosphere needs to be $< 700\mathrm{km}$, consistent with the H_2 densities from *Koskinen et al.* [2013]. The data are not consistent with a H corona of long scale height or high density (Sec. 3.2).

6. Proton measurements were used to constrain the water molecule column density of the bulk D-ring to $nH = 2 \times 10^{16}/\mathrm{m}^2$. This density is equivalent to an optical depth of $\tau \approx 4 \times 10^{-6}$ (Sec. 5).
7. The D72 ringlet absorbs protons as efficiently as the bulk of the D-ring, suggesting that ring and ringlet have a similar density despite their different optical appearance (Sec. 4.2).

Acknowledgments

Cassini/MIMI data and a user guide are available through NASA's planetary data system (PDS). Data taken after July 2017 will be added throughout 2018. The JHU/APL authors (PK, DGM, JC, GC, CP) are partially supported by the NASA Office of Space Science under task order 003 of contract NAS5-97271 between NASA/GSFC and JHU. The German contribution of the MIMI/LEMMS instrument, as well as ER and NK were in part financed by the German BMWi through the German Space Agency DLR under contracts 50 OH 0103, 50 OH 0801, 50 OH 0802, 50 OH 1101, 50 OH 1502, and by the Max Planck Society. The French participation in the Cassini project (AK) is funded by CNES. LHR contribution was supported by a NASA Living With a Star grant (NNX16AL12G). The authors like to thank A. Lagg (MPS) and J. Vandegriff (JHU/APL) for analysis software support, M. Kusterer (JHU/APL) for reducing the MIMI data, and Q. Nénon (ONERA) for useful discussions.

References

Adriani, O., G. C. Barbarino, G. A. Bazilevskaya, R. Bellotti, M. Boezio, E. A. Bogomolov, M. Bongi, V. Bonvicini, S. Bottai, A. Bruno, F. Cafagna, D. Campana, R. Carbone, P. Carlson, M. Casolino, G. Castellini, C. De Donato, C. De Santis, N. De Simone, V. Di Felice, V. Formato, A. M. Galper, A. V. Karelin, S. V. Koldashov, S. Koldobskiy, S. Y. Krutkov, A. N. Kvashnin, A. Leonov, V. Malakhov, L. Marcelli, M. Martucci, A. G. Mayorov, W. Menn, M. Mergé, V. V. Mikhailov, E. Mocchiutti, A. Monaco, N. Mori, R. Munini, G. Osteria, F. Palma, B. Panico, P. Papini, M. Pearce, P. Picozza, M. Ricci, S. B. Ricciarini, R. Sarkar, V. Scotti, M. Simon, R. Sparvoli, P. Spillantini, Y. I. Stozhkov, A. Vacchi, E. Vannuccini, G. I. Vasilyev, S. A. Voronov, Y. T. Yurkin, G. Zampa, N. Zampa, and V. G. Zverev (2015), Trapped Proton Fluxes at Low Earth Orbits Measured by the PAMELA Experiment, , *799*, L4, doi:10.1088/2041-8205/799/1/L4.

Burton, M. E., M. K. Dougherty, and C. T. Russell (2010), Saturn's internal planetary magnetic field, *Geophys. Res. Lett.*, *37*, L24105, doi:10.1029/2010GL045148.

Charnoz, S., L. Dones, L. W. Esposito, P. R. Estrada, and M. M. Hedman (2009), Origin and Evolution of Saturn's Ring System, in *Saturn from Cassini-Huygens*, edited by Dougherty, M. K., Esposito, L. W., & Krimigis, S. M., pp. 537–575, Springer Science+Business Media B.V., Heidelberg, Germany, doi:10.1007/978-1-4020-9217-6_17.

Clark, G., C. Paranicas, D. Santos-Costa, S. Livi, N. Krupp, D. G. Mitchell, E. Roussos, and W.-L. Tseng (2014), Evolution of electron pitch angle distributions across Saturn's middle magnetospheric region from MIMI/LEMMS, *Planet. Space Sci.*, *104*, 18–28, doi:10.1016/j.pss.2014.07.004.

Cooper, J. F. (1983), Nuclear cascades in Saturn's rings - Cosmic ray albedo neutron decay and origins of trapped protons in the inner magnetosphere, *J. Geophys. Res.*, *88*, 3945–3954, doi:10.1029/JA088iA05p03945.

Cooper, J. F. (2008), Innermost Van Allen Radiation Belt for High Energy Protons at Saturn, in *BAAS*, vol. 40(3), p. 460.

Garrett, H. B., M. Kokorowski, and I. jun (2012), Galileo Interim Radiation Electron Model Update - 2012, in *JPL Publication 12-9*.

Gladstone, G. R., W. R. Pryor, W. K. Tobiska, A. I. F. Stewart, K. E. Simmons, and J. M. Ajello (2004), Constraints on Jupiter's hydrogen corona from Galileo UVS observations, *Planet. Space Sci.*, *52*, 415–421, doi:10.1016/j.pss.2003.06.012.

Hartogh, P., E. Lellouch, R. Moreno, D. Bockelée-Morvan, N. Biver, T. Cassidy, M. Rengel, C. Jarchow, T. Cavalié, J. Crovisier, F. P. Helmich, and M. Kidger (2011), Direct detection of the Enceladus water torus with Herschel, *A&A*, *532*, L2, doi:10.1051/0004-6361/201117377.

Hedman, M. M., J. A. Burns, M. R. Showalter, C. C. Porco, P. D. Nicholson, A. S. Bosh, M. S. Tiscareno, R. H. Brown, B. J. Buratti, K. H. Baines, and R. Clark (2007), Saturn's dynamic D ring, *Icarus*, *188*, 89–107, doi:10.1016/j.icarus.2006.11.017.

Hedman, M. M., J. A. Burns, D. Nicholson, P, and J. N. Cuzzi (2013), Status report of dust hazards for f-ring/proximal orbits, *Cassini Project Science Group presentation*.

Hedman, M. M., J. A. Burt, J. A. Burns, and M. R. Showalter (2014), Non-circular features in Saturn's D ring: D68, *Icarus*, *233*, 147–162, doi:10.1016/j.icarus.2014.01.022.

Hess, W. N., E. H. Canfield, and R. E. Lingenfelter (1961), Cosmic-Ray Neutron Demography, *J. Geophys. Res.*, *66*, 665–677, doi:10.1029/JZ066i003p00665.

Kempf, S., U. Beckmann, G. Moragas-Klostermeyer, F. Postberg, R. Srama, T. Economou, J. Schmidt, F. Spahn, and E. Grün (2008), The E ring in the vicinity of Enceladus. I. Spatial distribution and properties of the ring particles, *Icarus*, *193*, 420–437, doi:10.1016/j.icarus.2007.06.027.

Kollmann, P., E. Roussos, C. Paranicas, N. Krupp, and D. K. Haggerty (2013), Processes forming and sustaining Saturn's proton radiation belts, *Icarus*, *222*, 323–341, doi:10.1016/j.icarus.2012.10.033.

Kollmann, P., E. Roussos, A. Kotova, J. F. Cooper, D. G. Mitchell, N. Krupp, and C. Paranicas (2015), MeV proton flux predictions near Saturn's D ring, *J. Geophys. Res.*, *120*, 8586–8602, doi:10.1002/2015JA021621.

Kollmann, P., P. C. Brandt, G. Collinson, Z. J. Rong, Y. Futaana, and T. L. Zhang (2016), Properties of planetward ion flows in Venus' magnetotail, *Icarus*, *274*, 73–82, doi:10.1016/j.icarus.2016.02.053.

Kollmann and Roussos et al. (2017), The evolution of Saturn's radiation belts modulated by changes in radial diffusion, *Nature Astronomy*, *1*, 872–877, doi:10.1038/s41550-017-0287-x.

Koskinen, T. T., B. R. Sandel, R. V. Yelle, F. J. Capalbo, G. M. Holsclaw, W. E. McClintock, and S. Edgington (2013), The density and temperature structure near the exobase of Saturn from Cassini UVIS solar occultations, *Icarus*, *226*, 1318–1330, doi:10.1016/j.icarus.2013.07.037.

Koskinen, T. T., B. R. Sandel, R. V. Yelle, D. F. Strobel, I. C. F. Müller-Wodarg, and J. T. Erwin (2015), Saturn's variable thermosphere from Cassini/UVIS occultations, *Icarus*, *260*, 174–189, doi:10.1016/j.icarus.2015.07.008.

Kotova, A., E. Roussos, P. Kollmann, N. Krupp, and I. Dandouras (2018), Galactic Cosmic Rays access to the magnetosphere of Saturn, , *submitted*.

Krimigis, S. M., D. G. Mitchell, D. C. Hamilton, S. Livi, J. Dandouras, S. Jaskulek, T. P. Armstrong, J. D. Boldt, A. F. Cheng, G. Gloeckler, J. R. Hayes, K. C. Hsieh, W.-H. Ip, E. P. Keath, E. Kirsch, N. Krupp, L. J. Lanzerotti, R. Lundgren, B. H. Mauk, R. W. McEntire, E. C. Roelof, C. E. Schlemm, B. E. Tossman, B. Wilken, and D. J. Williams (2004), Magnetosphere Imaging Instrument (MIMI) on the Cassini Mission to Saturn/Titan, *Space Sci. Rev.*, *114*, 233–329, doi:10.1007/s11214-004-1410-8.

Krupp, N., E. Roussos, P. Kollmann, D. G. Mitchell, C. P. Paranicas, S. M. Krimigis,

D. C. Hamilton, M. Hedman, and M. K. Dougherty (2018), Energetic neutral and charged particle measurements in the inner Saturnian magnetosphere during the Grand Finale orbits of Cassini 2016/2017, , *this issue*.

Nagy, A. F., A. J. Kliore, M. Mendillo, S. Miller, L. Moore, J. I. Moses, I. Müller-Wodarg, and D. Shemansky (2009), *Upper Atmosphere and Ionosphere of Saturn*, p. 181, Springer Science+Business Media B.V., Heidelberg, Germany, doi:10.1007/978-1-4020-9217-6_8.

Roederer, J. G. (1970), *Dynamics of Geomagnetically Trapped Radiation*, Springer Verlag, Heidelberg, Germany.

Roussos, E., N. Krupp, T. P. Armstrong, C. Paranicas, D. G. Mitchell, S. M. Krimigis, G. H. Jones, K. Dialynas, N. Sergis, and D. C. Hamilton (2008), Discovery of a transient radiation belt at Saturn, *Geophys. Res. Lett.*, *35*, 22,106, doi:10.1029/2008GL035767.

Roussos, E., N. Krupp, C. P. Paranicas, P. Kollmann, D. G. Mitchell, S. M. Krimigis, T. P. Armstrong, D. R. Went, M. K. Dougherty, and G. H. Jones (2011), Long- and short-term variability of Saturn's ionic radiation belts, *J. Geophys. Res.*, *116*(A15), A02,217, doi:10.1029/2010JA015954.

Roussos and Kollmann et al. (2018), Relativistic protons trapped between Saturn and its rings, *Science*, *under review*.

Rymer, A. M., B. H. Mauk, T. W. Hill, C. Paranicas, D. G. Mitchell, A. J. Coates, and D. T. Young (2008), Electron circulation in Saturn's magnetosphere, *J. Geophys. Res.*, *113*(A12), 1201, doi:10.1029/2007JA012589.

Seidelmann, P. K., B. A. Archinal, M. F. A'Hearn, A. Conrad, G. J. Consolmagno, D. Hestroffer, J. L. Hilton, G. A. Krasinsky, G. Neumann, J. Oberst, P. Stooke, E. F. Tedesco, D. J. Tholen, P. C. Thomas, and I. P. Williams (2007), Report of the IAU/IAG Working Group on cartographic coordinates and rotational elements: 2006, *Celestial Mechanics and Dynamical Astronomy*, *98*, 155–180, doi:10.1007/s10569-007-9072-y.

Selesnick, R. S., J. B. Blake, and R. A. Mewaldt (2003), Atmospheric losses of radiation belt electrons, *J. Geophys. Res.*, *108*, 1468, doi:10.1029/2003JA010160.

Selesnick, R. S., D. N. Baker, A. N. Jaynes, X. Li, S. G. Kanekal, M. K. Hudson, and B. T. Kress (2014), Observations of the inner radiation belt: CRAND and trapped solar protons, *Journal of Geophysical Research (Space Physics)*, *119*, 6541–6552, doi:10.1002/2014JA020188.

Shemansky, D. E., and X. Liu (2012), Saturn upper atmospheric structure from Cassini EUV and FUV occultations11This article is part of a Special Issue that honours the work of Dr. Donald M. Hunten FRSC who passed away in December 2010 after a very illustrious career., *Canadian Journal of Physics*, *90*, 817–831, doi:10.1139/p2012-036.

Shemansky, D. E., X. Liu, and H. Melin (2009), The Saturn hydrogen plume, , *57*, 1659–1670, doi:10.1016/j.pss.2009.05.002.

Strobel, D. (2015), Update of SAMWG proximal mission planning: modeling Saturn's upper atmosphere, *Saturn Atmosphere Working Group presentation*.

Van Allen, J. A., B. A. Randall, and M. F. Thomsen (1980), Sources and sinks of energetic electrons and protons in Saturn's magnetosphere, , *85*, 5679–5694, doi:10.1029/JA085iA11p05679.

Walt, M. (1994), *Introduction to geomagnetically trapped radiation*, 1st ed., Cambridge University Press, Cambridge, United Kingdom.

Ziegler, J. F. (2008), SRIM 2008, free software, `http://www.srim.org`.

Figure 1.

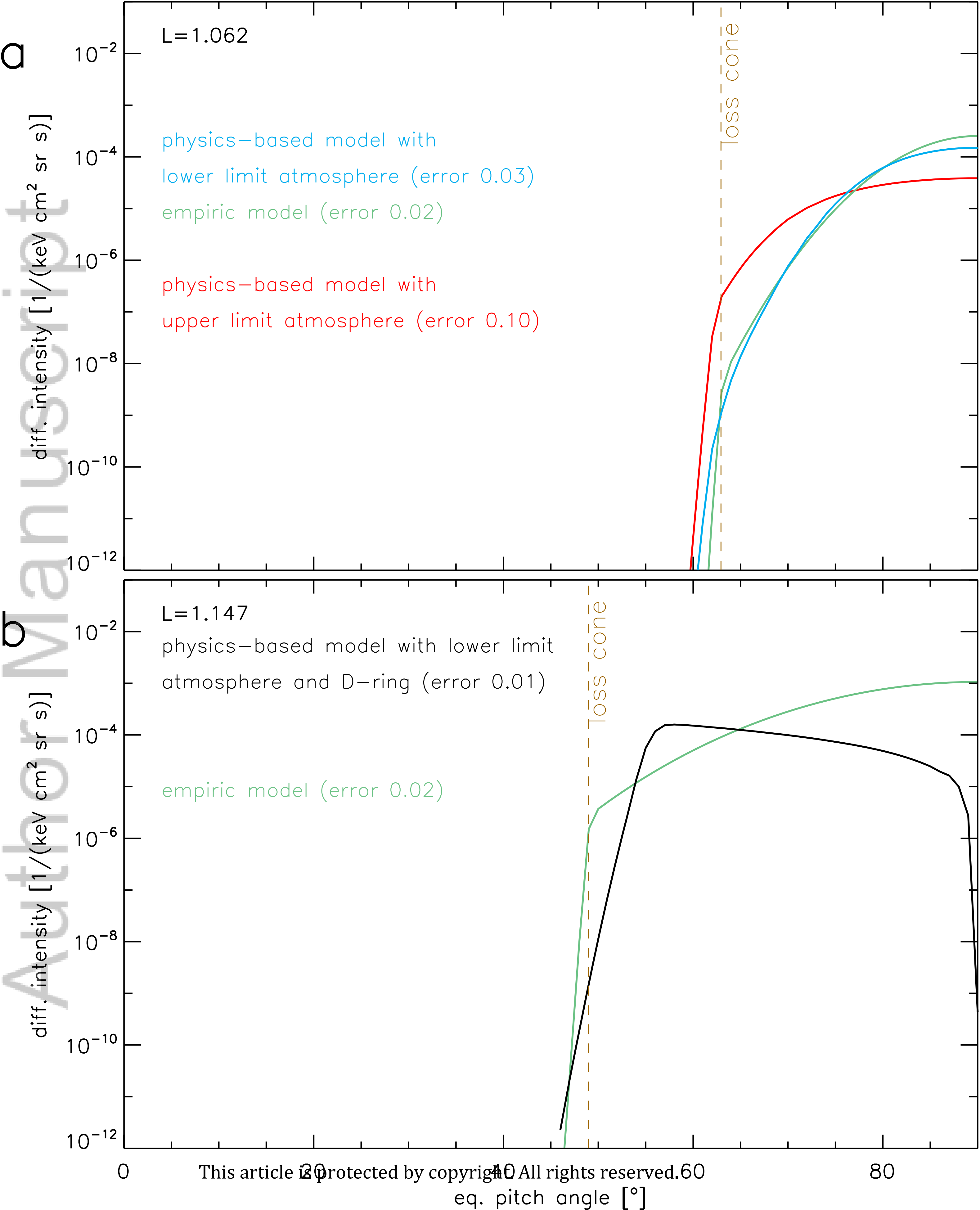
a
L=1.062
physics−based model with
lower limit atmosphere (error 0.03)
empiric model (error 0.02)
physics−based model with
upper limit atmosphere (error 0.10)
loss cone
b
L=1.147
physics−based model with lower limit
atmosphere and D−ring (error 0.01)
empiric model (error 0.02)
loss cone
diff. intensity [1/(keV cm² sr s)]
eq. pitch angle [°]
0
20
40
60
80

Figure 2.

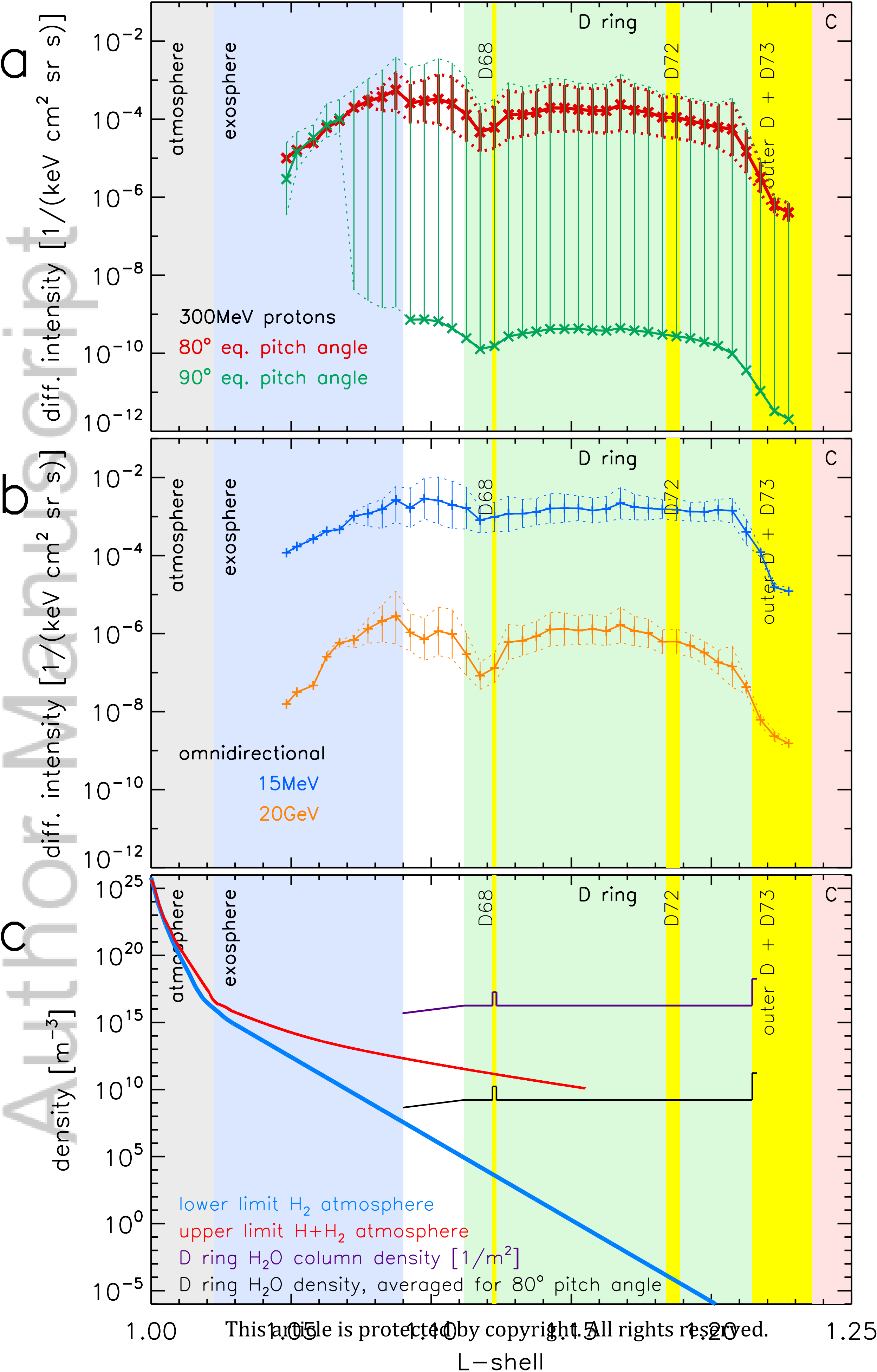

a
b
c
atmosphere
exosphere
D ring
C
D68
D72
outer D + D73
diff. intensity [1/(keV cm² sr s)]
300MeV protons
80° eq. pitch angle
90° eq. pitch angle
omnidirectional
15MeV
20GeV
density [m⁻³]
lower limit H₂ atmosphere
upper limit H+H₂ atmosphere
D ring H₂O column density [1/m²]
D ring H₂O density, averaged for 80° pitch angle
1.00
1.05
1.10
1.15
1.20
1.25
L−shell

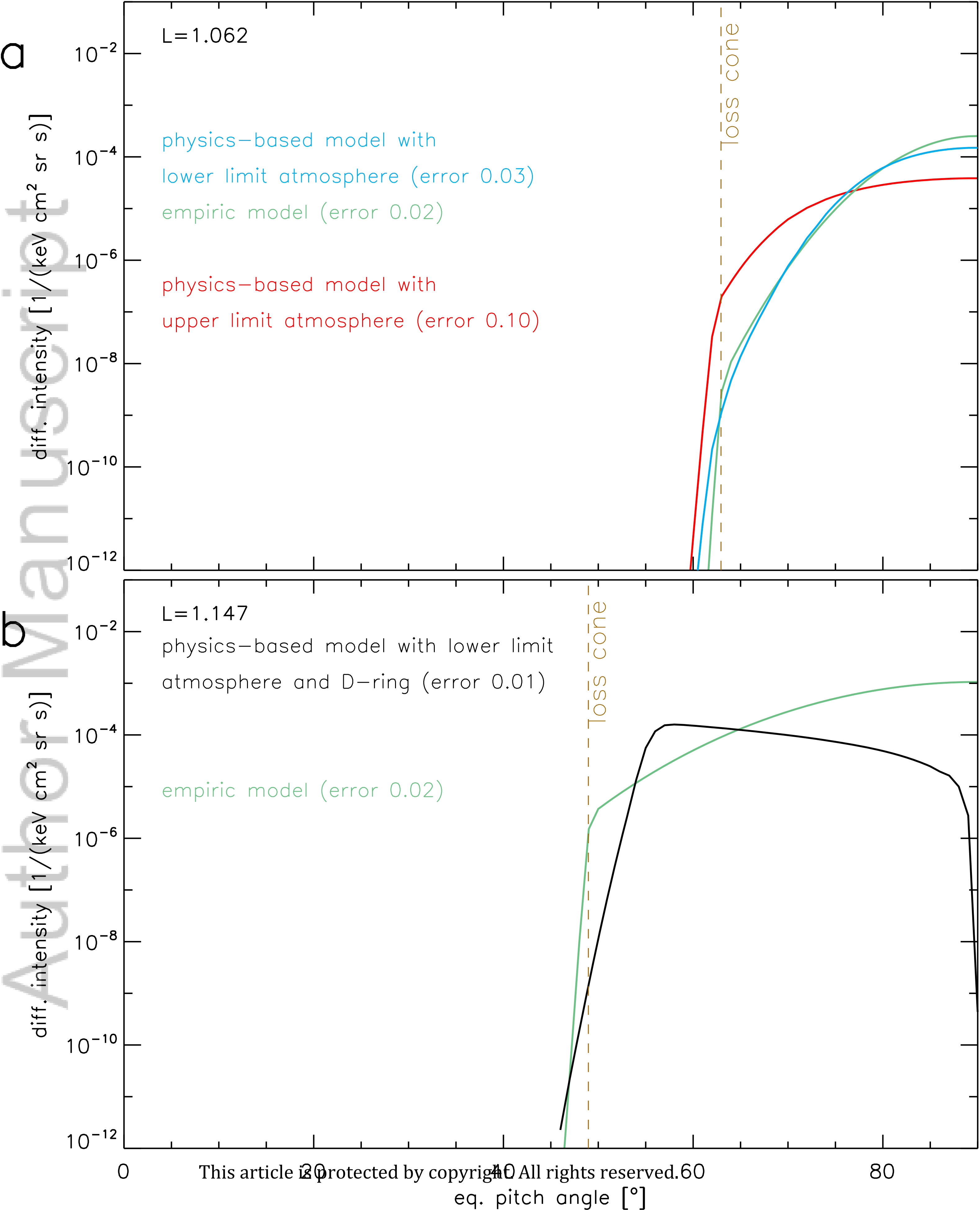
a
b
L=1.062
physics−based model with
lower limit atmosphere (error 0.03)
empiric model (error 0.02)
physics−based model with
upper limit atmosphere (error 0.10)
loss cone
L=1.147
physics−based model with lower limit
atmosphere and D−ring (error 0.01)
empiric model (error 0.02)
loss cone
diff. intensity [1/(keV cm² sr s)]
eq. pitch angle [°]
0
20
40
60
80

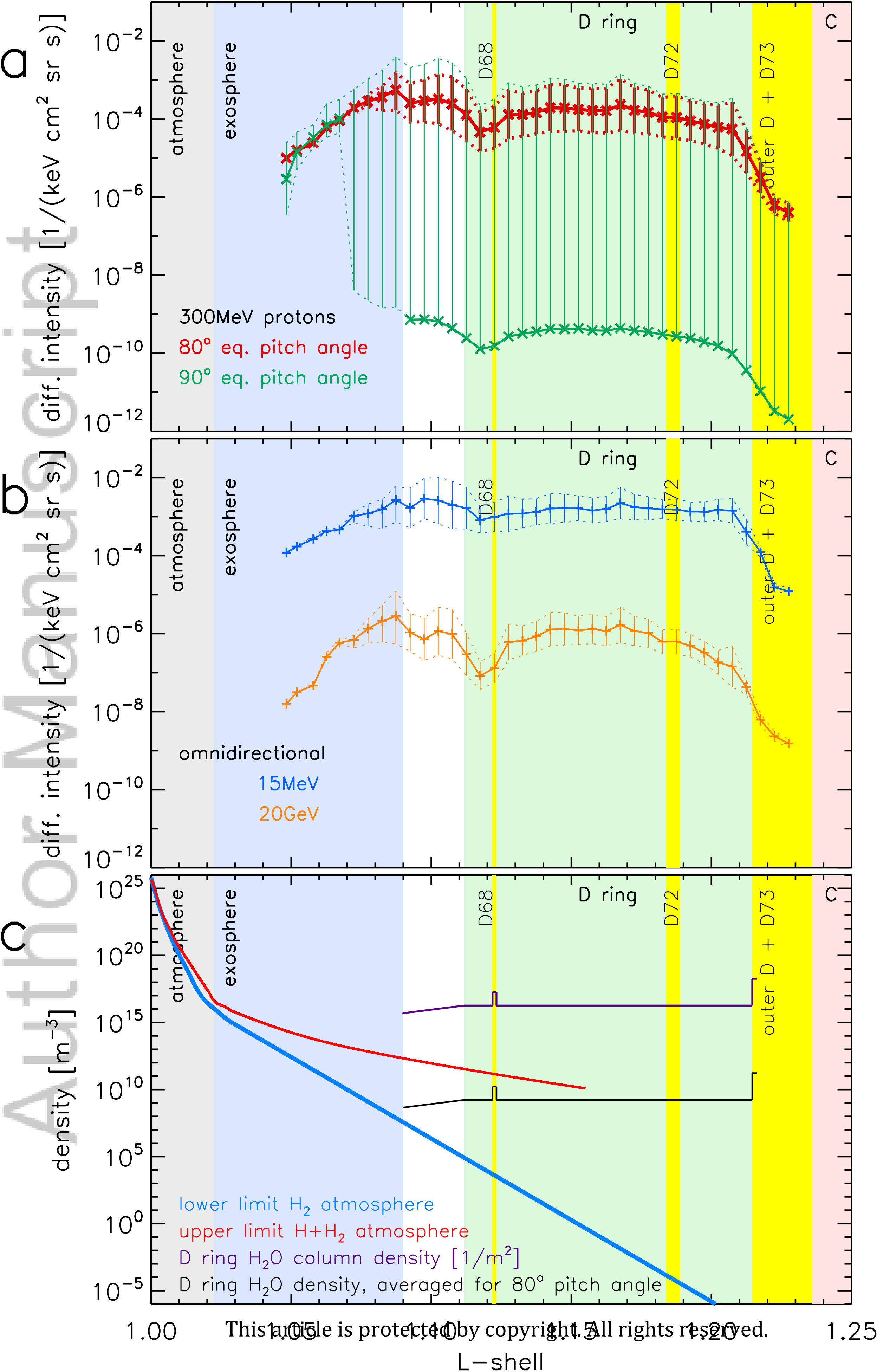
a
b
c
atmosphere
exosphere
D ring
C
D68
D72
outer D + D73
diff. intensity [1/(keV cm^2 sr s)]
300MeV protons
80° eq. pitch angle
90° eq. pitch angle
omnidirectional
15MeV
20GeV
density [m^{-3}]
lower limit H_2 atmosphere
upper limit $H+H_2$ atmosphere
D ring H_2O column density [1/m^2]
D ring H_2O density, averaged for 80° pitch angle
1.00
1.05
1.10
1.15
1.20
1.25
L−shell